Computers and Chemical Engineering 198 (2025) 109083

Contents lists available at ScienceDirect

Computers and Chemical Engineering

journal homepage: www.elsevier.com/locate/cace

# Application of a temporal multiscale method for efficient simulation of degradation in PEM Water Electrolysis under dynamic operating conditions

Dayron Chang Dominguez [a,*], An Phuc Dam [b], Shaun M. Alia [c], Thomas Richter [a], Kai Sundmacher [a,b]

[a] Institute for Analysis and Numerics, Otto-von-Guericke University, Universitätsplatz 2, Magdeburg, 39106, Saxony-Anhalt, Germany
[b] Department Process Systems Engineering, Max–Planck-Institute for Dynamics of Complex Technical Systems, Sandtorstr. 1, Magdeburg, 39106, Saxony-Anhalt, Germany
[c] Chemical and Material Sciences Center, National Renewable Energy Laboratory, 15013 Denver West Parkway, Golden, 80401, CO, United States of America

ARTICLE INFO

*Keywords:*
Temporal multiscale method
Electrochemical modeling
PEM Electrolysis
Heterogeneous multiscale method
Differential equations

ABSTRACT

Hydrogen is emerging as a vital energy carrier, driven by the need to reduce carbon emissions. Proton Electrolyte Membrane Water Electrolysis (PEMWE) enables hydrogen production under fluctuating renewable power conditions but requires improved understanding and stability of the anode catalyst layer under dynamic operating conditions, especially with low noble metal loadings. Long-term degradation experiments are both time-consuming and costly; therefore, a systematic, model-aided approach is essential. In the present work, a temporal multiscale method is applied to reduce the computational effort of simulating long-term degradation processes in PEMWE, with an exemplary focus on catalyst dissolution. A mechanistic model incorporating the oxygen evolution reaction, catalyst dissolution, and hydrogen permeation from the cathode to the anode was hypothesized and implemented. In this way, the local periodicity of transport and reaction processes in dynamic PEMWE operation, which influence the gradual degradation of the catalyst layer, is captured. The temporal multiscale method significantly reduces the computational effort of simulation, decreasing processing time from hours to mere minutes. This efficiency gain is attributed to the limited evolution of Slow-Scale variables during each period of time P of the Fast-Scale variables. Consequently, simulation is required only until local periodicity is achieved within each Slow-Scale time step. Hence, the fully resolved dynamic problem is decoupled into these two scales, employing a heterogeneous multiscale technique. The developed approach effectively accelerates parameter estimation and predictive simulations, supporting systematic modeling of PEMWE degradation under dynamic conditions.

## 0. Introduction

Degradation of the anode catalyst layer (ACL) is a major challenge in Proton Exchange Membrane Water Electrolysis (PEMWE), especially due to the need to reduce loadings of noble metal materials such as iridium (Ir). Understanding the degradation phenomena that occur within the ACL of the PEM Water Electrolyzer (Prestat, 2023; Dam et al., 2023) is challenging due to the "black-box" nature of such a PEMWE cell during operation, even more so under dynamically changing load conditions (Voronova et al., 2022). Insights are typically gained by studying the system's in-output behavior as well as by conducting post-test analysis of the system.

In situ experimental knowledge regarding the phenomenon of Ir catalyst dissolution has been acquired through the use of so-called half-cell setups, where liquid electrolytes are employed, and models are validated (Qian et al., 2022). However, obtaining similar in situ data is challenging for the industrially relevant membrane electrode assembly (MEA) setups. Transfer of knowledge of catalyst dissolution from half-cells to full-cells is not straight forward (Dam et al., 2020; Knöppel et al., 2021).

Therefore, mathematical modeling is of essential importance to understand the physico-chemical processes occurring inside the cell. Since the early 2000s modeling processes in PEMWEs has been used as a tool to make up for shortfalls in such a closed devices (Grigor'ev et al., 2001; Onda et al., 2002). An extensive classification of different ways of modeling PEMWE can be found in Olivier et al. (2017). Some are focused on the understanding of the phenomena under various conditions such as high-pressure water electrolysis (Grigoriev et al., 2010; Yigit and Selamet, 2016) or hydrogen permeation (Trinke et al.,

* Corresponding author.
*E-mail address:* dayron.dominguez@ovgu.de (D.C. Dominguez).

https://doi.org/10.1016/j.compchemeng.2025.109083
Received 16 January 2025; Received in revised form 10 February 2025; Accepted 28 February 2025
Available online 10 March 2025

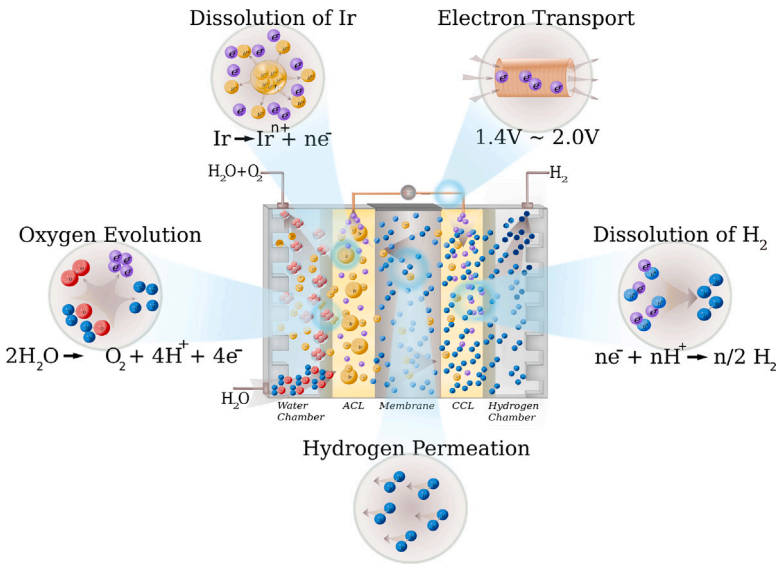


**Fig. 1.** Theoretical schema of the processes of the PEMWE that are taken into consideration in the proposed model.

2016; Papakonstantinou and Sundmacher, 2019; Franz et al., 2023). Additionally, models ranging from 0D to 3D of PEMWEs have been developed based on physical laws to describe mechanisms such as mass transport (Abdol Rahim et al., 2016; Aubras et al., 2017) and fluid behavior through the Porous Transport Layer (PTL) (Ojong et al., 2017; Doan et al., 2021; Lin and Zausch, 2023; Ni et al., 2023) among others.

In the area of performance characterization and control system development, there are works like (Gorgun, 2006; Marangio et al., 2009; Lebbal and Lecøeuche, 2009; Espinosa-López et al., 2018; Ogumerem and Pistikopoulos, 2020; Dizon et al., 2021), mainly focused on analysis of experimental results and long-term durability evaluation. The authors utilized fitting techniques based on experimental data to identify parameters and optimize the performance of PEMWEs using often "black-box" models. In this regard, the machine learning era unfolds data-driven simulating techniques which accelerate the fitting processes due to their computational efficiency (Ding et al., 2022).

Models have been developed for PEMWE in which multiscale analysis has applied in order to better resolve the spatial dimensions (Franco et al., 2007; Franco and Gerard, 2008; Franco et al., 2009; Oliveira et al., 2012). In this study a white-box methodology for modeling the catalyst dissolution phenomena inside the PEMWE ACL shall be developed (Fig. 1). This will be numerically supported by applying a temporal multiscale method in order to reduce computational effort.

This technique has been used to describe long-term effects in the interaction of processes of different time scales in different applications as is shown by Yang et al. (2016) and Brinkmann et al. (2018). In this way, the Heterogeneous Multiscale Method (HMM) (Weinan and Engquist, 2003) is one of the most promising options to efficiently decouple the micro-scale and macro-scale of the problem solving the last one based on temporal averaging of the first one. A review of these techniques can be found in Weinan et al. (2007), Gravemeier et al. (2008) where authors compare the HMM with other techniques, mainly applied for ODEs or to spatial multiscales.

In Frei and Richter (2020) a description of a computational temporal multiscale method is derived. It assumes that the underlying fast process has a time quasi-locally periodic solution if the influence of the Slow-Scale solution is fixed during the slow time step. Therefore, only solving the Fast-Scale variables until such a time quasi-locally periodic is achieved allows the Slow-Scale variables to have very large time steps which accelerates the simulations by about $10^4$ times.

In this paper a simple physico-chemical model of iridium catalyst dissolution is proposed in Section 1. It is shown that with the introduction of a numerical temporal multiscale method in Section 2, the simulation time of the PEMWE ACL long-duration stability tests is drastically reduced. In Section 3 the method is numerically analyzed showing how to overcome the challenges of the stiffness nature of the problem. The model parameters are fitted to experimental data of two dynamic operation profiles (Alia et al., 2019) of accelerated stress tests (see Section 4). A good fit of model simulation with experimental data is achieved. The model with the fitted parameters is then used to predict other dynamic operation profiles. The simulation is compared to experimental data and implications on the hypothesized electrochemical model are discussed.

Overall, the aim of this work is to demonstrate how the introduction of a temporal multiscale approach, facilitates the systematic development of a mathematical model capable of describing the effects of different dynamic operational profiles on catalyst degradation in PEMWE.

## 1. Anode catalyst layer degradation model

In this section, the electrochemical degradation model of the ACL during the operation of the PEMWE is described. The catalyst dissolution model is presented in Section 1.1, and an important influence of hydrogen is assumed, as it can chemically reduce the Ir oxide, thus leading to its destabilization during dynamic operation of PEMWE (Papakonstantinou and Sundmacher, 2019; Weißet al., 2019). Therefore, a transport model has been developed and implemented to describe the dynamic permeation process of hydrogen from the cathode to the anode side which will be discussed in Section 1.2.

### 1.1. Iridium dissolution model

To describe the dissolution process of Ir, based on knowledge and understanding from previous works in literature, a simple mechanistic model is hypothesized and implemented. The model considers nanoparticles of iridium in which the catalyst material surface can be in two different chemical oxidation states as shown in Fig. 2. They can be either in a reduced or an oxidized state. $\Theta_1$ and $\Theta_2$ correspond to the more reduced and the more oxidized state, respectively.

Fig. 2 illustrates the schematic of iridium dissolution model which was implemented in this work. It is well known that catalyst dissolution and OER are closely coupled phenomena. An unstable state of the catalyst surface during the OER reaction cycle leads to catalyst dissolution (Kasian et al., 2018; Geiger et al., 2018; Dam et al., 2020).

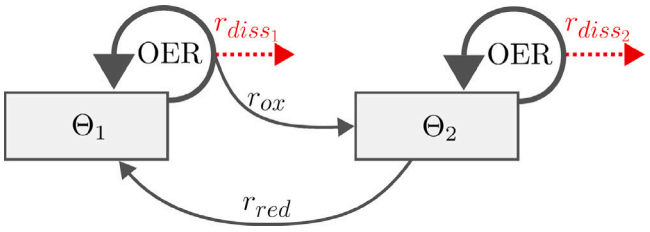


**Fig. 2.** Theoretical representation of the electrochemical model for corrosion of the material in the ACL.

In this model it is assumed that the surface is generally in an oxidized state during the considered operation of PEMWE at OER potentials. However, hydrogen which permeates from the cathode to the anode side can reduce the oxidation state of the active site on the catalyst surface. Thus, this reduction converts it from the state $\Theta_2$ to the state $\Theta_1$ ('$r_{red}$').

Nevertheless, the OER leads to dissolution of those chemically reduced active sites. As a result, the Ir oxide lattice structure underneath the dissolved catalyst species becomes exposed to the surface. The surface state $\Theta_1$ then reverts back towards the more stable state $\Theta_2$ ('$r_{ox}$'). However, the dissolution of catalyst species leads to a loss of catalyst material leading to a loss of the Electrochemical Surface Area (ECSA) and a gradual decline in electrolyzer performance over time.

The catalyst surface in state $\Theta_2$ is more stable than in state $\Theta_1$. However, due to the inherent coupling of catalyst dissolution and OER (Binninger et al., 2015; Kasian et al., 2018), the catalyst can dissolved also in the former state. Therefore, two dissolution pathways are considered in the implemented model, as shown in Fig. 2.

The involvement of hydrogen in the dissolution of catalyst material may influence the observed ACL degradation rates. This is especially notable under different dynamic operation conditions, as these conditions strongly influence the dynamic behavior of oxygen and hydrogen partial pressure in the ACL. A high current density results in a low hydrogen partial pressure as evolved oxygen generates a flushing effect on the ACL. On the other hand, the decrease in current density leads to a dynamic accumulation of hydrogen in the ACL, attributable to the prior storage of permeating hydrogen within the membrane.

The implemented mathematical model can be expressed by the following system of ordinary differential (ODE) equations:

$$\frac{d\Theta_1}{dt} = 2k_r(1-\Theta_1)^2\left(C_{H_2}^{ACL}RT\right) - \frac{\Theta_1}{\gamma}k_{diss_1}e^{fE^{ACL}} \tag{1}$$

$$\frac{dC_{O_2}^{ACL}}{dt} = V_{ACL}^{-1}\left[\frac{i}{z_{O_2}F} - A_{geo}F_{O_2}^{PTL}\right] \tag{2}$$

$$\frac{dC_{H_2}^{ACL}}{dt} = \frac{A_{geo}}{V_{ACL}}\left[F_{H_2}^{Mem} - F_{H_2}^{PTL}\right] \tag{3}$$

$$\frac{dN_{Ir}^{np}}{dt} = -\frac{A_{Ir}^{act}(N_{Ir}^{np}(t))}{A_{geo}}\left[\Theta_1 k_{diss_1} + (1-\Theta_1)k_{diss_2}\right]e^{fE^{ACL}} \tag{4}$$

The origin and meaning of the variables and terms in this system of ODEs shall be described in the following sections. $\Theta_1$ stands for the fraction of active sites which are in state number 1 (see 2). The first term of (1) expresses the reduction rate with its reaction rate constant $k_r$.

The reduction kinetics depends on the pressure of hydrogen in the ACL since it occurs via chemical reduction with hydrogen and is written via elementary reaction kinetic formulation. The modeled reduction process may be described formally by the stoichiometric reaction equation $2IrO_2 + H_2 \rightarrow 2HIrO_2$. The hydrogen partial pressure is calculated from the ideal gas law:

$$P_{H_2}^{ACL} = C_{H_2}^{ACL}RT, \tag{5}$$

with $R$ and $T$ being the universal gas constant and the temperature, respectively. $C_{H_2}^{ACL}$ is the concentration of hydrogen in the ACL and is given in $mol/m^3$. The hydrogen-induced reduction reaction leads to a conversion of active sites from state $\Theta_2$ to the state $\Theta_1$.

On the other hand, the right-hand side term of Eq. (1) represents the conversion of sites in state $\Theta_1$ back to the state $\Theta_2$. This is explained by the dissolution of reduced and destabilized sites, exposing the Ir oxide species that were originally located underneath the dissolving sites. $k_{diss_1}$ is the dissolution rate constant for the sites in $\Theta_1$ state. $\gamma$ is the number of active sites per surface area of the Ir oxide nano-particles and a value of $1.121\times10^{-4}\,mol/m^2$ is used for the simulation (Papakonstantinou et al., 2022). $E^{ACL}$ is the potential applied on the ACL, and $f = F/(RT)$, where $F$ is the Faraday's constant, i.e. 96485 C/mol.

In terms of spatial dimensions, the ACL is modeled zero-dimensionally. The balance of the gases it is shown in the Eqs. (2) and (3). The $O_2$ concentration is balanced by a source and a flow term. Within the source term, $i$ represents the current density ($A/m^2$) and $z_{O_2}$ is equal to 4, corresponding to the number of electrons transferred per evolved oxygen molecule. The other term of Eq. (2) defines the flow of $O_2$ from the ACL to the porous space inside the adjacent PTL domain. These fluxes can be described by:

$$F_{O_2}^{PTL} = F^{tot}X_{O_2} \quad \text{and} \quad F_{H_2}^{PTL} = F^{tot}X_{H_2}, \tag{6}$$

where $F^{tot}$ is the total gas flow out of the ACL and $X_{O_2}$ and $X_{H_2}$ are the oxygen and the hydrogen fraction in the gas phase, respectively. These fractions can be calculated by:

$$X_{O_2} = \frac{P_{O_2}^{ACL}}{P_{H_2}^{ACL} + P_{O_2}^{ACL}} \quad \text{and} \quad X_{H_2} = \frac{P_{H_2}^{ACL}}{P_{H_2}^{ACL} + P_{O_2}^{ACL}}. \tag{7}$$

The total gas flow $F^{tot}$ is calculated using the following equation:

$$F^{tot} = k_{ACL}\left(\left(P_{O_2}^{ACL} + P_{H_2}^{ACL}\right) - P^{atm}\right). \tag{8}$$

The pressure difference serves as the mechanical driving force for the gas flow out of the ACL. The parameter $k_{ACL}$ is a mass transport coefficient and its inverse describes the resistance of gas transport out of the ACL domain. Although, in reality, this transport resistance is distributed spatially across the ACL thickness, for the sake of simplicity, this work assumes discrete occurrence at the interface between the ACL and PTL domains.

A value of $k_{ACL}$ can be determined using the Darcy–Weisbach equation, assuming a pore diameter of 52 nm (Alia et al., 2019) and a correction for the friction factor of 0.005 (Liu et al., 2012). An ACL thickness of 1 μm is assumed for the ACL with low catalyst loading (Alia et al., 2019). $P^{atm}$ is the atmospheric pressure which can be considered as the pressure level inside the pores of the PTL domain.

Eq. (3) considers output and input flows. The outflow is defined as $F_{H_2}^{PTL}$ in Eq. (6). The input flow $F_{H_2}^{Mem}$ which comes from the membrane domain will be explained in the following Section 1.2.

Eq. (4) describes the temporal evolution of the amount of Ir in the form of nanoparticles ($N_{Ir}^{np}$ measured in moles) within the ACL due to the two previously described dissolution mechanisms. The ECSA, defined by $A_{Ir}^{act}$, is calculated based on

$$A_{Ir}^{act} = \eta_{np}^{act}4\pi r_{np}^2 \quad \text{and} \quad r_{np} = \sqrt[3]{\frac{3N_{Ir}^{np}M_{Ir}}{4\pi\rho_{Ir}\eta_{np}^{act}}}. \tag{9}$$

The variable $\eta_{np}^{act}$ represents the number of active nanoparticles, while the radius $r_{np}$ denotes their size. Additionally, parameters such as the molar mass of Iridium, denoted as $M_{Ir}$ (in [g/mol]), and its density $\rho_{Ir}$ (in [g/m3]) are present in the formulation.

In the kinetics a linearity between Ir catalyst dissolution and OER at higher current densities is included. This linearity results in the same factor in front of the potential within the exponent of the rate expression.

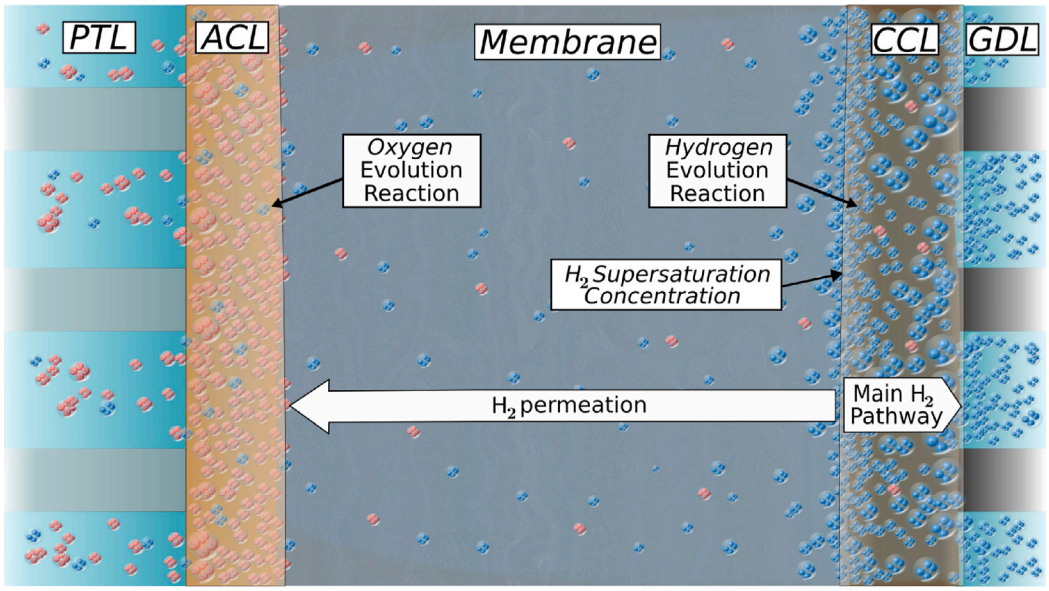


**Fig. 3.** The sketch shows a section of the PEMWE consisting of the membrane in the middle and the two catalyst layers (ACL, CCL) at either side of the membrane. In the cathode catalyst layer most of the evolved hydrogen is transported to the cathode outlet. However, a small fraction of hydrogen permeates through the membrane towards the anode side. In the ACL, oxygen is evolved and a small volumetric fraction is constituted by hydrogen.

### 1.2. Transport of hydrogen through the membrane

Due to the electrochemical polarization of the catalyst layer, hydrogen is evolved in the CCL. In previous studies, it has been found that this creates a supersaturation of hydrogen in the CCL, resulting not only in the transport of hydrogen in the cathode channel direction but also the permeation of hydrogen to the anode side (Trinke et al., 2017). This is schematically shown in Fig. 3. In this work, the transport is modeled via a partial differential equation which considers the time-dependent diffusion of hydrogen over the membrane domain as

$$\partial_t C_{H_2}^{MEM}(x,t) - D_{H_2}^{eff}\partial_{xx} C_{H_2}^{MEM}(x,t) = 0. \tag{10}$$

The PDE is discretized and solved using the Finite Element Method in a one-dimensional domain, considering $D_{H_2}^{eff}$ as the effective hydrogen diffusion coefficient of the membrane.

The boundary condition at the CCL side was implemented as a Dirichlet boundary condition. For simplicity, this can be done by assuming quasi-steady-state conditions at the CCL and therefore calculating the supersaturation concentration based on the following equation (Trinke et al., 2017):

$$C_{H_2}^{CCL}(t) = \frac{\frac{i}{2F} + k_l C_{H_2}^{Henry}(t)}{k_l + \frac{D_{H_2}^{eff}}{\delta^{MEM}}}. \tag{11}$$

On the rhs, the first term of the numerator represents the $H_2$ evolution which depends on the current density $i$. For the mass transfer coefficient $k_l$, which describes the transport from the reaction local to the cathode GDL domain, a value of $10^{-4}$ m/s is used, taken from the same literature. $C_{H_2}^{Henry}$ is the theoretical saturation concentration of dissolved hydrogen calculated from Henry's law in the absence of mass transfer limitations. The membrane $\delta^{MEM}$ is considered one-dimensionally in space and discretized from 0 to the membrane thickness of $L = 183$ µm.

On the other side, the boundary conditions for the membrane and the ACL are defined via Neumann boundary conditions

$$D_{H_2}^{eff}\partial_x C_{H_2}^{MEM}(0,t) = k_{H_2}^{MEM} RT\left(C_{H_2}^{MEM}(0,t) - C_{H_2}^{ACL}(t)\right). \tag{12}$$

For the mass transfer coefficient $k_{H_2}^{MEM}$ (unit 1/m) a very high value of $10^{-10}$ is chosen and therefore, effectively, the resistance directly at the interface between the membrane and the ACL domain is considered negligible. Note that the entire equation has been divided by the diffusion coefficient, which is consequently combined into the model parameter $k_{H_2}^{MEM}$.

The factor $RT$ comes from the original definition of the transport rate coefficient, which is based on the pressure difference as the driving force. The ideal gas law, as given by Eq. (5), can be used to express the same term via the concentration difference. $C_{H_2}^{MEM}(0,t)$ is the estimated concentration of hydrogen at the first element of the discretized membrane over time and the concentration inside the ACL is given by the variable $C_{H_2}^{ACL}$. The flux between the membrane and the ACL $F_{H_2}^{Mem}$ in Eq. (3) is calculated by:

$$F_{H_2}^{Mem}(t) = k_{H_2}^{MEM} RT(C_{H_2}^{MEM}(0,t) - C_{H_2}^{ACL}(t)). \tag{13}$$

This relationship is employed to couple both problems: the ACL modeled by an ODE system and membrane domain by a PDE. The coupling is achieved through a Fixed Point Iteration Method as explained in Section 3.

## 2. Temporal multiscale method for solving the degradation model

Upon closer examination of the complete problem described by Eqs. (1)–(4), (10) a difference in time scales between Eq. (4) and the others becomes noticeable. The process of dissolution, in fact, takes hours to undergo a measurable change in its state. In contrast, the remaining equations describe very fast processes as kinetics (represented by $\Theta_1$ and $\Theta_2$) and the changes in the concentrations of $O_2$ and $H_2$ in the ACL. As a matter of effect, those occur in time lapses less than a second.

The assumed magnitudes for the mentioned equations are responsible for the time scale distinctions. The first term of (1) is approximately $10^{-11}$ taking into account that $k_r \approx 10^{-14}$, $0 \leqslant \Theta_1 \leqslant 1$ and the maximum value of $C_{H_2}^{ACL}$ is approximately 0.5 bar. The second term has a magnitude of $10^{-12}$ due to $k_{diss_1} \approx 10^{-25}$, resulting in a total magnitude of $10^{-12}$ for the entire equation. In the case of Eq. (4), the constant $k_{diss_2}$ is assumed to be around $10^{-37}$, resulting in a total magnitude of approximately $10^{-5}$.

Therefore, there exists a proportionality between the variables which can be approximated by $\varepsilon \approx 10^{-7}$. This reveals an underlying temporal multiscale structure of the complete problem, as proposed

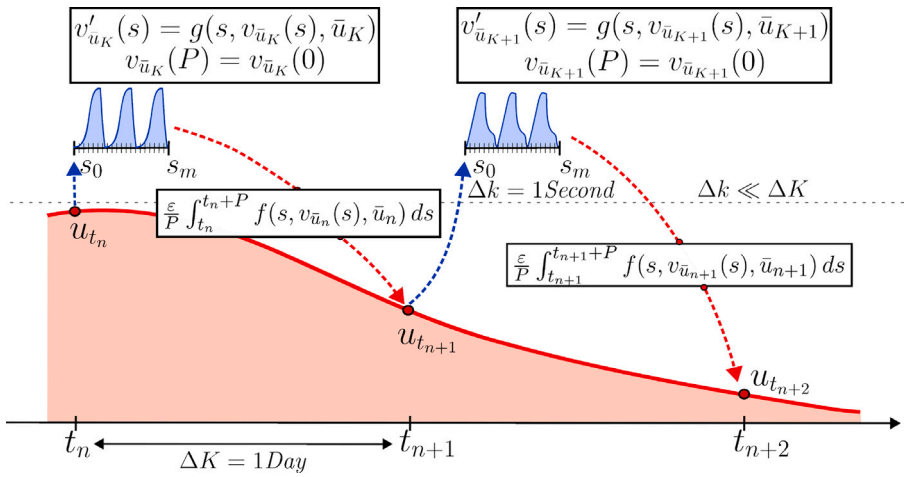


**Fig. 4.** Scheme of the temporal multiscale method. In each Slow-Scale time step $t_n$ local quasi-periodic Fast-Scale solutions $v_{\bar{u}_K}$ are computed by fixing the averaged Slow-Scale solution $\bar{u}_K$ over a period $P$. Then the solution of the Slow-Scale at the next time step $t_{n+1}$ is computed through averaging the Slow-Scale equation $f$ over the local quasi-periodic interval $P$ utilizing the Fast-Scale variable solutions.

by Weinan (2011), with variables categorized into Fast-Scale and Slow-Scale from Eqs. (1)–(3), (10) and (4) respectively. Furthermore, the Slow-Scale is $O(1)$ with respect to the Fast-Scale through $\varepsilon$.

Moreover, the Fast-Scale processes also display a local quasi-periodic behavior due to the input of the potential. If the slow variable would not further evolve, a periodic-in-time forcing would result in a periodic response. Thus, these profiles simulate the oscillatory behavior resulting from real-world degradation of PEMWEs in operation. Then, during a $P$ period of time there are not significant changes of the Slow-Scale variables.

A direct simulation of such a temporal multiscale problem is not efficient. Resolving the complete time interval with time steps of less than a second (e.g. $\Delta k = 10^{-2}$ s) would result in excessive computational effort although the slow process, which is the one of most interest, is hardly changing. We therefore utilize a temporal multiscale algorithm that is based on the heterogeneous multiscale method (Weinan and Engquist, 2003; Abdulle et al., 2012) and that aims at decoupling slow and fast scale.

The first step of decoupling is to derive an effective equation by averaging the slow process (4) over one period $P$. Second, instead of resolving the fast process dynamically in time, it is localized by fixing the slow variable $N_{\mathrm{Ir}}^{np}$ and by replacing the Fast-Scale feedback by the periodic-in-time limit cycle of ((1) - (3), (10)) which can be numerically approximated without simulating the complete history of the fast scale variables. By this decoupling, a temporal multiscale method is obtained that allows to step forward the coupled temporal multiscale problem with very large time-steps. We refer to Frei and Richter (2020), and Lautsch and Richter (2021) for details (see Fig. 4).

Taking advantage of this particular structure of the problem and the theory of averaging of the multiscale problems it is possible to approximate the complete problem with its corresponding temporal multiscale problem as in the next Section 2.1 will be explained.

### 2.1. Temporal multiscale method

Based on the stated, the Slow-Scale variables of the approximated temporal multiscale problem are defined over $t \in [0, T] \subset \mathbb{R}$ having $\Delta K$ as a large time step size. In the case of the Fast-Scale variables, if $P$ is established as the period and $0 \leqslant m \leqslant (T - \Delta K)/\Delta K$, then these variables will be defined over $s \in [t_K + \Delta K + nP, t_K + \Delta K + (n+1)P]$ for $0 \leqslant n \leqslant (\Delta K - P)/P$ and $t_K = m\Delta K$ with a small time step size $\Delta k \ll \Delta K$. The new problem is written as follows:

Find $\bar{N}_{\mathrm{Ir}}^{np}(t)$ that approximates $N_{\mathrm{Ir}}^{np}(t)$ and is the solution of

$$\frac{d\bar{N}_{\mathrm{Ir}}^{np}}{dt} = -\frac{\varepsilon}{P}\int_{t_K+nP}^{t_K+(n+1)P} \frac{A_{\mathrm{Ir}}^{\mathrm{act}}}{A_{geo}}\left[\hat{\Theta}_1(s)\, k_{\mathrm{diss}_1} + \left(1 - \hat{\Theta}_1(s)\right) k_{\mathrm{diss}_2}\right] e^{fE^{\mathrm{ACL}}(s)}\, ds \tag{14}$$

so that for all $K$ there exists $n \in \mathbb{N}_0$ and the interval $[t_K + nP, t_K + (n+1)P] \subset [t_K, t_{K+1}]$ such that the equations of the Fast-Scale

$$\frac{d\hat{\Theta}_1(s)}{ds} = 2k_r(1 - \hat{\Theta}_1(s))^2\left(\hat{C}_{\mathrm{H}_2}^{\mathrm{ACL}}(s)\, RT\right) - \frac{\hat{\Theta}_1(s)}{\gamma} k_{\mathrm{diss}_1} e^{fE^{\mathrm{ACL}}(s)} \tag{15}$$

$$\frac{d\hat{C}_{O_2}^{\mathrm{ACL}}(s)}{ds} = \frac{A_{\mathrm{Ir}}^{\mathrm{act}}\left(\bar{N}_{\mathrm{Ir}}^{np}(t)\right)}{V_{\mathrm{ACL}}}\left[\frac{i}{z_{O_2}F} - F_{O_2}^{PTL}(s)\right] \tag{16}$$

$$\frac{d\hat{C}_{\mathrm{H}_2}^{\mathrm{ACL}}(s)}{ds} = \frac{A_{\mathrm{geo}}}{V_{\mathrm{ACL}}}\left[F_{\mathrm{H}_2}^{\mathrm{Mem}}(s) - F_{\mathrm{H}_2}^{\mathrm{PTL}}(s)\right] \tag{17}$$

$$\partial_s \hat{C}_{\mathrm{H}_2}^{\mathrm{MEM}}(x, s) = D_{\mathrm{H}_2}^{\mathrm{eff}} \partial_{xx} \hat{C}_{\mathrm{H}_2}^{\mathrm{MEM}}(x, s), \tag{18}$$

with the same initial conditions as the complete problem, are satisfied in each chosen interval and their solution is locally quasi-periodic.

The choice of $\Delta K$ is conditioned by the prior choice of $\Delta k$ and the previously calculated scaling constant $\varepsilon$, such that $\Delta K \approx \Delta k/\varepsilon$. In this case, $\Delta k$ is set to $10^{-2}$ seconds to ensure stability over the Fast-Scale resolution. Since the experimental data used for validation was sampled in days, it was convenient to choose $\Delta K = 1$ day, which is approximately $10^5$ s and satisfies the mentioned temporal scale relation.

In order to simplify the notation some new symbols have been included. The $\hat{(\cdot)}$ accent will be understood as the average of the function, in this case the Slow-Scale variable. On the other hand, $\bar{(\cdot)}$ will represent the dependency

$$\hat{\upsilon} = (\hat{\Theta}_1, \hat{C}_{O_2}^{\mathrm{ACL}}, \hat{C}_{\mathrm{H}_2}^{\mathrm{ACL}}, \hat{C}_{\mathrm{H}_2}^{\mathrm{MEM}}) \tag{19}$$

in which function $\upsilon$ could be any of the Fast-Scale variables (in case of variable $\hat{C}_{\mathrm{H}_2}^{\mathrm{MEM}}$, $x$ is also included).

## 3. Numerical implementation

The numerical solution of the proposed problem in Section 2 is achieved by the implementation of the general temporal multiscale method shown in Algorithm 1.

The main idea is to solve the Fast-Scale problem using a *semi-implicit* method with a fixed $u_K$ solution over the interval $[t_K, t_K + \Delta K]$, until it reaches a locally quasi-periodic solution $\hat{\upsilon}_{u_K}$ with an error tolerance

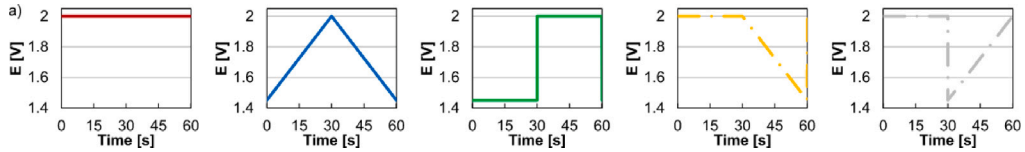


**Fig. 5.** Experimental data of five test profiles acquired from Alia et al. (2019). They are named from left to right: hold, triangle-wave, square-wave, sawtooth-up and sawtooth-down profiles.

**Algorithm 1** General temporal multiscale method for PEMWE dissolution problem

**Require:** $u_K = \bar{N}_{Ir}^{np}(t_0), \hat{v}_{u_K} = v_0$

1: **for** $K = 0, \ldots, N-1$ **do**

2: *Find the solution of the Fast-Scale equations* $\hat{v}_{u_K}$ *with fixed* $u_K$ *such that for* $n > 0$:

$||\hat{v}_{u_K}(t_K + nP) - \hat{v}_{u_K}(t_K + (n+1)P)|| < tolp$

3: *Find* $u_{K+1}$ *integrating the average of the Slow-Scale equation in the interval of the Fast-Scale solutions* $\hat{v}_{u_K}$ *such that:*

$u_{K+1} = u_K - \frac{\epsilon \Delta K}{P} \int_{t_K+nP}^{t_K+(n+1)P} \left[\hat{\Theta}_1(s)\, k_{\text{diss}_1} + \left(1 - \hat{\Theta}_1(s)\right) k_{\text{diss}_2}\right] e^{f E^{\text{ACL}}(s)}\, ds$

4: **end for**

5: **return** $u_{K+1}$

$\|tolp\|_\infty$. Then, the periodicity convergence criteria is defined as the infinite norm of the component-wise absolute errors for each Fast-Scale variable of the ACL. After that, $u_{K+1}$ is obtained by integrating the averaged Slow-Scale equation over the time interval which $\hat{v}_{u_K}$ is defined.

In order to solve the Fast-Scale problem the ODE System (15)–(17) coupled to the Transport Problem (18) must be solved. The solution of the Transport Problem was achieved by the application of a one dimensional time implicit Finite Element Method. Approximation of integrals of the mass and stiffness matrices were carried out by applying the trapezoidal method. For time integration the implicit backward Euler method was implied.

On the other hand, due to the stiff features of the problem, the ODE System mentioned before was solved applying an second-order backward differentiation formula scheme implemented in the 'ode' function of the 'integrate' module of the scientific computing library 'scipy' (Virtanen et al., 2020), available in the Python programming language. Back in Section 1, it was explained how hydrogen coming from the membrane could drastically permeate the ACL, and this is precisely what causes a jump in the solutions, making it more difficult to solve with explicit methods, which will need time step adaptivity and therefore longer computation time.

Coupling both problems in each time step $\Delta k$ was accomplished by first solving the ODE system (15)–(17) implicitly with step size $\Delta k$, keeping $u_K$ and $\hat{C}_{H_2}^{\text{MEM}}(t_K)$ fixed. Afterwards, the Transport Problem (18) is solved considering the solutions of the system (15)–(17) corresponding to $t_K$ and $t_{K+1}$. Once a locally quasi-periodic solution $\hat{v}_{u_k}$ is found, then the Slow-Scale equation is integrated. The integration method used for this purpose is the Adams–Bashforth second order method.

## 4. Results and discussion

The dynamic operation profiles, as well as experimental data, are taken from Alia et al. (2019). The cyclic voltammetric charge, which was systematically measured in this work, is used as a metric for the electrochemical surface area of the PEMWE device. In this experimental investigation, five dynamic operation profiles were applied in which the cell potential was controlled (Fig. 5). These long-term experiments were conducted for 525 h of operation.

**Table 1**
Computational time and mean squared error (MSE) of the results for the fully resolved problem and the temporal multiscale method (FRP and TMS) across the five experimental profiles (Alia et al., 2019) for 21 simulated days.

| Experiment profiles | Computational time | | $\text{MSE}(N_{\text{Ir}}^{\text{np}}, \bar{N}_{\text{Ir}}^{\text{np}})$ |
|---|---|---|---|
| | FRP (days) | TMS (min) | |
| Hold | 8.6 | 19.09 | $7.87 \times 10^{-06}$ |
| Square-wave | 6.8 | 13.29 | $2.46 \times 10^{-04}$ |
| Triangle-wave | 6.4 | 13.46 | $5.39 \times 10^{-06}$ |
| Sawtooth Down | 8.0 | 16.84 | $3.00 \times 10^{-05}$ |
| Sawtooth Up | 8.2 | 21.06 | $5.52 \times 10^{-04}$ |

### 4.1. Temporal multiscale simulation

A comparison between the fully-resolved and the temporal multiscale problems was made to verify the accuracy of the approximation that could be achieved with the multiscale approach. The simulations were run to cover 21 days of operation of the PEMWE with initial ECSA $= 3.25 \times 10^{-2}\,\text{m}^2$, period of 60 s and, as was shown in Section 2.1, $\Delta k$ and $\Delta K$ are chosen as $10^{-2}$ seconds and 24 h respectively.

In Table 1, the results of this comparison, considering the already fitted parameters, are tabulated. From it, we see that the average ratio of computational time between these two methods is approximately 2.82 orders of magnitude, which means that the temporal multiscale method is around thousand times faster than the fully-resolved one on average. The best computational time for the fully-resolved problem is about 6.4 days, which, compared with the 21 minutes that the longest temporal multiscale simulation took, represents a significant computational reduction. Thus, approximately 1.25 simulation days are computed per 1 minute of computation for the temporal multiscale method. These experiments were carried out in a computer equipped with a Intel(R) Core(TM) i7-7700 CPU running at 3.60 GHz with a system memory of 16 GB. Memory consumption is negligible.

The maximum mean squared error between these two sets of simulation results is approximately $5.52 \times 10^{-4}$, which is very small considering the enormous computational reduction made. This shows that the temporal multiscale method is accurate enough to be used instead of the fully-resolved one for approximating the long-term effects of the dissolution of Iridium when a PEMWE is operated. This property is ideal for estimating parameters efficiently as will be shown in Section 4.2.

### 4.2. Parameter fitting

Regarding fitting the parameters of the model, a single set of parameters $k_r$ and $k_{\text{diss}_2}$, was estimated using data obtained from hold and square-wave profiles. The data from the other profiles was used as a test set. The objective function of the resulting optimization problem is expressed as

$$\sigma^* = \arg \min_{\sigma \in \Omega \subset \mathbb{R}^2} \frac{1}{T} \int_0^T (S_{\text{HP}}(t) - u_{\text{HP}}(t;\sigma))^2 + (S_{\text{SWP}}(t) - u_{\text{SWP}}(t;\sigma))^2\, dt, \quad (20)$$

where $\Omega$ is the space of feasible solutions of the form $\sigma = (k_r, k_{\text{diss}_2})$, $S_{\text{HP}}$ and $S_{\text{SWP}}$ the sampled data from hold and square-wave profile and $u$ the Slow-Scale variable for each case.

For the fitting procedure, a variant of the Simulating Annealing Optimization Method called Simple Serializable Set from Greening (1990)

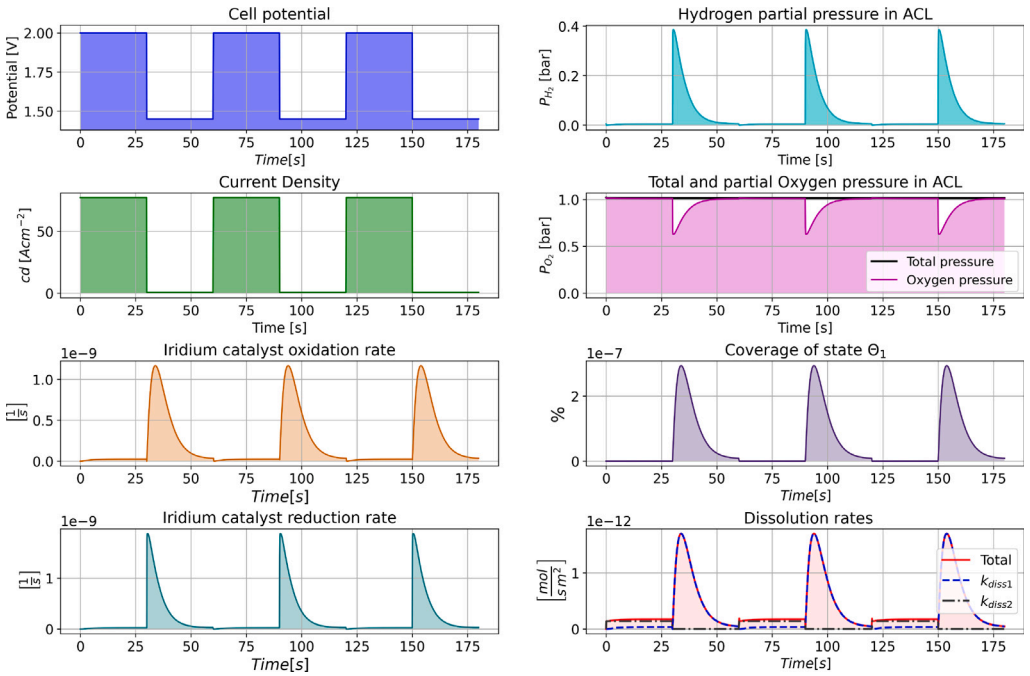


**Fig. 6.** Fast-Scale variables for the square-wave profile simulation for the first 3 periods ($0 \leq t \leq 180$ s).

was applied. In this way, a compute server with 2 AMD EPYC 7662 CPUs running at 2.15 GHz and 2 TB of memory was used to widely spread the search around partial solutions, running 128 simultaneous simulations for each set of parameters in the search neighborhood for each iteration of the method. At the end of the fitting procedure the values $k_r^* = 2.437792 \times 10^{-14}$ and $k_{\text{diss}_2}^* = 1.947001 \times 10^{-37}$ have been identified. The mean squared errors of Table 1 show the achieved accuracy.

### 4.3. Evaluation of the model performance with experimental data

Multiple output variables were obtained for each Fast-Scale variable. The Fast-Scale variables of the hold profile exhibit steady-state behavior almost throughout the entire duration. To provide a more insightful comparison, the results of the square-wave profile are presented in Figs. 6 and 7, as this profile, along with the Hold profile, was chosen for fitting the model parameters.

In Fig. 6, abrupt changes in all variables are observable at every period, specifically at 30 s after the start of each. These changes result from sudden drops in the applied cell potential, which is also the source of the *stiffness* discussed in Sections 1 and 3.

With respect to the transport of hydrogen in the membrane, Fig. 7 illustrates various stages of hydrogen concentration profile during the last period shown in Fig. 6. Graphs (a) and (b) indicate the build up of the pressure during the rise of potential up to 1.45 V. An initial stage of potential drop is shown in (c), where the hydrogen concentration decreases in the CCL due to the drop in current density. In (d), the amount of hydrogen stored in the membrane has been almost completely transported out. Finally, in (e) a high current density was restarted, and the entire process repeats itself.

The Slow-Scale variables are presented in Fig. 8. It is illustrated how the ECSA decays over time for experimental data and the model simulation. It can be observed that, through the described fitting procedure, a single set of parameters has been obtained. The use of the latter results in a good agreement between the simulation and experimental data for both the hold and square-wave operation profiles. Only a slight bending up observed in the experimental data of the hold profile does not seem to be well captured by the implemented model. This may indicate that a mechanism leading to the stabilization of the catalyst under steady-state conditions of the hold profile has been neglected by the model. However, apart from this aspect, based on the minimized low root mean squared error, a successful model fitting and therefore parameter estimation was achieved.

This set of parameters is then employed to predict the outcome of the other three PEMWE operation profiles that are presented in Fig. 5 (triangle, sawtooth-up and sawtooth-down). The model simulations and the corresponding data are presented in Fig. 8 (b). The model predictions show a significant deviation from the experimental data, indicating the need for further development and improvement of the mechanistic degradation model. In particular, the model appears to underestimate the degradation effect of the slower, dynamic ramps of the triangular and the two sawtooth operation profiles.

Finding the perfect electrochemical model which fits all the dynamic operation profiles shown is out of the scope of this work. However, it is shown how the application of the temporal multiscale approach can lead to a much faster simulation of long-term degradation processes in PEMWE.

A systematic model development can be performed by iterating the following steps: (1) proposing/modifying the mathematical degradation model, (2) applying the parameter fitting procedure, (3) performing predictive simulations and (4) comparing the predictive simulations with the experimental data. The temporal multiscale approach can play an important role in this iterative process by facilitating the simulation and especially the parameter estimation step. Once a reliable degradation model is found, the temporal multiscale approach can also be used to optimize the dynamic operation of PEMWE, taking into account the long-term degradation effects of different dynamic operating strategies.

## Conclusion and future perspectives

In this work, a temporal multiscale method was applied to accelerate simulation of degradation in PEMWE under dynamic operating conditions. With an exemplary focus on the phenomenon of catalyst dissolution, a mechanistic degradation model was hypothesized and implemented. Due to the specific underlying temporal multiscale structure of the fully-resolved problem, its computational complexity was reduced by solving a temporal multiscale equivalent problem.

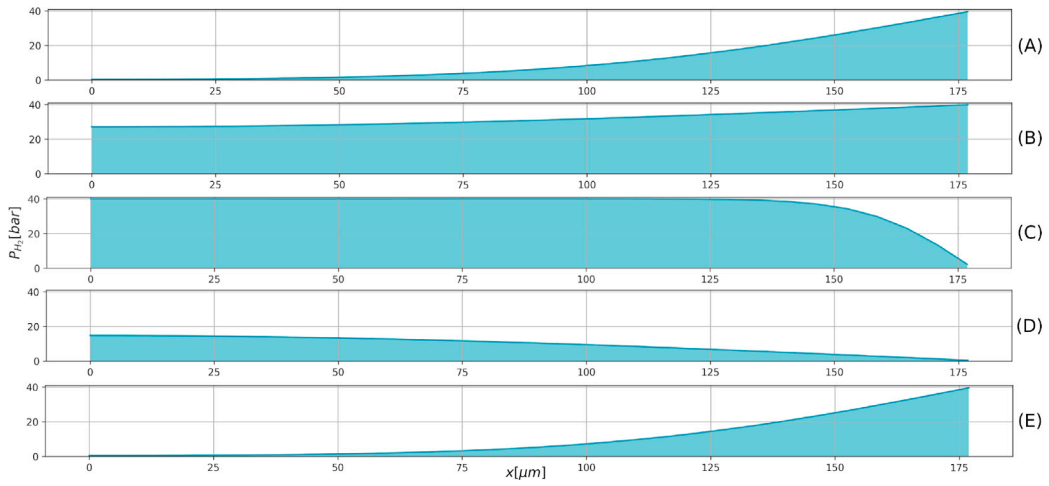


**Fig. 7.** The Fast-scale solutions of the hydrogen transport problem in the membrane for the period $t \in [120, 180]$ s. The graph (a) is the state of the concentration of hydrogen at $t = 120$ s, (b) at $t = 125$ s, (c) at $t = 150$ s, (d) at $t = 155$ s and (e) at $t = 180$ s respectively.

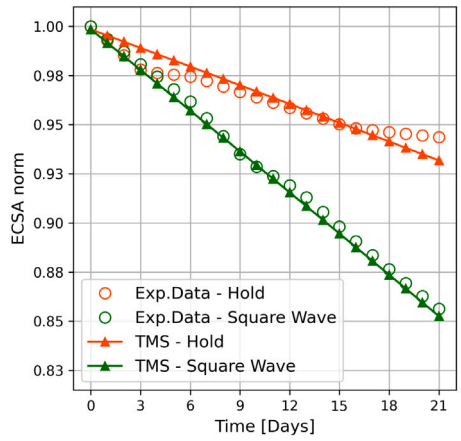


(a) Parameter estimation step: Normalized ECSA data from Alia et al. (2019) vs the simulated results from the model with the application of the temporal multiscale method (TMS) for hold and square-wave profiles.

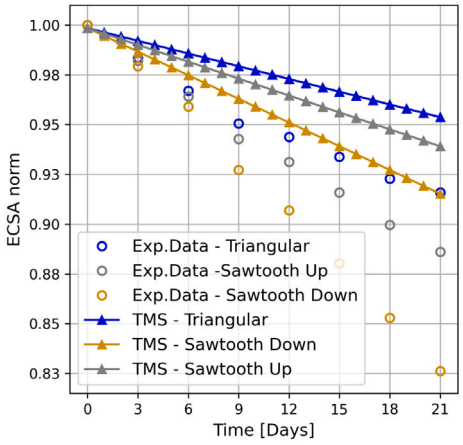


(b) Model prediction step: Normalized ECSA data from Alia et al. (2019) vs the simulated results from the model with the application of the temporal multiscale method (TMS) for triangular, sawtooth-up and down profiles.

**Fig. 8.** Slow-Scale variables results compared with the experimental data provided by Alia et al. (2019) after 21 days of simulation.

In this regard, two different temporal scales were identified: A fast process with quasi-local periodicity dictated by the transport and reaction processes occurring under intermittent operation conditions of PEMWE, and a slow process constituted by the gradual degradation of the catalyst layer.

Assuming that the Slow-Scale variables are minimally affected by the Fast-Scale variables in a time step significantly larger than the one used for the time discretization of the Fast-Scale variables, we can consider the Slow-Scale variables as fixed during the computation of the Fast-Scale solution. Additionally, the presented temporal multiscale method leverages the quasi-local periodicity of the Fast-Scale variables not computing all the time steps but rather the necessary ones to achieve such periodicity. This enables the integration of the Slow-Scale variable solution over the mentioned large time step, utilizing the Fast-Scale variables solutions for just one period of time to compute the gradient.

The computational effort is substantially reduced compared to the fully-resolved problem solution. The temporal multiscale method, as mentioned before, does not require computing all the Fast-Scale solutions but only up to reaching a quasi-local periodicity for each Slow-Scale large time step. This makes it possible to reduce simulations covering 21 real time days from 8 computational days for the fully-resolved problem to approximately 20 min. Furthermore, the mean squared error committed by the temporal multiscale method is approximately $10^{-5}$, making the impact of the assumptions negligible in terms of accuracy.

Numerical challenges, such as the stiffness of the Fast-Scale problem, were overcome by applying an implicit integration method using the Newton method. A semi-implicit integration method was also employed to ensure the stability of the coupling between the hydrogen transport and the ACL degradation problem.

The model parameters were fitted using a Simulating Annealing algorithm. Although a gradient descent method was not utilized as the optimization method for the parameter fitting to avoid additional errors from applying a finite difference method for small values, the temporal multiscale approach proposed in this work also contributed to accelerating this procedure. Since the simulations took significantly less time than before, a wider search space of possible fitting solutions was explored. For this purpose, 128 simultaneous simulations were run for each iteration of the Simulating Annealing Method, resulting in a

better approximation to the optimal parameters for fitting this problem. This could be replaced in the future by a fitting method that directly considers the particular temporal multiscale structure of the problem.

The model parameters were estimated by fitting the model to the experimental data of two operation profiles ('hold' and 'square-wave') in PEMWE, resulting in a close agreement between the model simulation and the experimental data. However, the model prediction of the three other operation profiles of the cell potential ('triangular', 'sawtooth-up' and 'sawtooth-down') shows significant deviations from the experimental data, indicating the need for further modification of the mathematical degradation model.

In this paper, it is shown that the application of the temporal multiscale method can support the systematic development of a degradation model in PEMWE by drastically reducing the computational time for the model fitting and predictive simulation steps. In the future, the application of the temporal multiscale method can also aid to realize efficient numerical methods that can be used to optimize the dynamic operation and the model-based control of PEMWE.

## CRediT authorship contribution statement

**Dayron Chang Dominguez:** Writing – original draft, Visualization, Software, Project administration, Methodology, Investigation, Formal analysis, Conceptualization. **An Phuc Dam:** Writing – review & editing, Validation, Software, Resources, Methodology, Investigation, Formal analysis, Conceptualization. **Shaun M. Alia:** Writing – review & editing, Validation, Investigation, Formal analysis, Data curation. **Thomas Richter:** Writing – review & editing, Validation, Supervision, Resources, Methodology, Investigation, Funding acquisition, Formal analysis, Conceptualization. **Kai Sundmacher:** Writing – review & editing, Validation, Supervision, Resources, Methodology, Investigation, Funding acquisition, Formal analysis, Conceptualization.

## Declaration of competing interest

The authors declare the following financial interests/personal relationships which may be considered as potential competing interests: Dayron Chang Dominguez reports financial support was provided by European Regional Development Fund. An Phuc Dam reports financial support was provided by European Regional Development Fund. Dayron Chang Dominguez reports financial support, administrative support, and article publishing charges were provided by International Max Planck Research School for Advanced Methods in Process and Systems Engineering. An Phuc Dam reports financial support was provided by Max Planck Society. Thomas Richter reports financial support was provided by German Research Foundation. Dayron Chang Dominguez reports financial support was provided by Ministry for Science, Energy, Climate Protection and the Environment of the State of Saxony-Anhalt. An Phuc Dam reports financial support was provided by Ministry for Science, Energy, Climate Protection and the Environment of the State of Saxony-Anhalt. Kai Sundmacher reports financial support was provided by Ministry for Science, Energy, Climate Protection and the Environment of the State of Saxony-Anhalt. Thomas Richter reports financial support was provided by Ministry for Science, Energy, Climate Protection and the Environment of the State of Saxony-Anhalt. Shaun M. Alia reports financial support was provided by Alliance for Sustainable Energy LLC. Shaun M. Alia has patent #1505121-1 with royalties paid to IOP Publishing, Ltd. If there are other authors, they declare that they have no known competing financial interests or personal relationships that could have appeared to influence the work reported in this paper.

## Acknowledgments

The research of Dayron Chang Dominguez and An Phuc Dam is supported by EU-program ERDF (European Regional Development Fund) of the German Federal State Saxony-Anhalt within the Research Center of Dynamic Systems (CDS) for financial support. Additionally, the work of Dayron Chang Dominguez is support by the International Max Planck Research School for Advanced Methods in Process and Systems Engineering (IMPRS ProEng), Magdeburg, Germany. The financial support of the MaxNet Energy research consortium of the Max Planck Society is by An Phuc Dam gratefully acknowledged.

The work of Thomas Richter has been supported by the Deutsche Forschungsgemeinschaft (DFG, German Research Foundation) as part of the GRK 2297 MathCore - 314838170, as well within the project 411046898.

This work is also part of the research initiative "SmartProSys: Intelligent Process Systems for the Sustainable Production of Chemicals" funded by the Ministry for Science, Energy, Climate Protection and the Environment of the State of Saxony-Anhalt.

Finally, this work was authored in part by the National Renewable Energy Laboratory, United States, operated by Alliance for Sustainable Energy, LLC, for the U.S. Department of Energy (DOE) under Contract No. DE-AC36-08GO28308. The views expressed in the article do not necessarily represent the views of the DOE or the U.S. Government. The U.S. Government retains and the publisher, by accepting the article for publication, acknowledges that the U.S. Government retains a nonexclusive, paid-up, irrevocable, worldwide license to publish or reproduce the published form of this work, or allow others to do so, for U.S. Government purposes.

## Data availability

Data will be made available on request.

## References

Abdol Rahim, A.H., Tijani, Alhassan Salami, Kamarudin, S.K., Hanapi, S., 2016. An overview of polymer electrolyte membrane electrolyzer for hydrogen production: Modeling and mass transport. J. Power Sources (ISSN: 03787753) 309, 56–65. http://dx.doi.org/10.1016/j.jpowsour.2016.01.012, URL https://linkinghub.elsevier.com/retrieve/pii/S037877531630012X.

Abdulle, Assyr, Weinan, E., Engquist, Björn, Vanden-Eijnden, Eric, 2012. The heterogeneous multiscale method. Acta Numer. (ISSN: 1474-0508) 21, 1–87. http://dx.doi.org/10.1017/S0962492912000025, ISSN: 0962-4929, URL https://www.cambridge.org/core/journals/acta-numerica/article/heterogeneous-multiscale-method/35814CB7A04B2EEAB9D173C48C6A9D6B. Publisher: Cambridge University Press.

Alia, Shaun M., Stariha, Sarah, Borup, Rod L., 2019. Electrolyzer durability at low catalyst loading and with dynamic operation. J. Electrochem. Soc. (ISSN: 0013-4651) 166 (15), F1164–F1172. http://dx.doi.org/10.1149/2.0231915jes, ISSN: 1945-7111, URL https://iopscience.iop.org/article/10.1149/2.0231915jes.

Aubras, F., Deseure, J., Kadjo, J.-J.A., Dedigama, I., Majasan, J., Grondin-Perez, B., Chabriat, J.-P., Brett, D.J.L., 2017. Two-dimensional model of low-pressure PEM electrolyser: Two-phase flow regime, electrochemical modelling and experimental validation. Int. J. Hydrog. Energy (ISSN: 03603199) 42 (42), 26203–26216. http://dx.doi.org/10.1016/j.ijhydene.2017.08.211, URL https://linkinghub.elsevier.com/retrieve/pii/S0360319917335565.

Binninger, Tobias, Mohamed, Rhiyaad, Waltar, Kay, Fabbri, Emiliana, Levecque, Pieter, Kötz, Rüdiger, Schmidt, Thomas J., 2015. Thermodynamic explanation of the universal correlation between oxygen evolution activity and corrosion of oxide catalysts. Sci. Rep. (ISSN: 2045-2322) 5 (1), 12167. http://dx.doi.org/10.1038/srep12167, URL https://www.nature.com/articles/srep12167. Number: 1 Publisher: Nature Publishing Group.

Brinkmann, F., Mercker, M., Richter, T., Marciniak-Czochra, A., 2018. Post-Turing tissue pattern formation: Advent of Mechanochemistry. PLoS Comput. Biol. http://dx.doi.org/10.1371/journal.pcbi.1006259.

Dam, An Phuc, Abuthaher, Bassam Y.A., Papakonstantinou, Georgios, Sundmacher, Kai, 2023. Insights into the path-dependent charge of iridium dissolution products and stability of electrocatalytic water splitting. J. Electrochem. Soc. (ISSN: 1945-7111) 170 (6), 064504. http://dx.doi.org/10.1149/1945-7111/acd4f2, Publisher: IOP Publishing.

Dam, An Phuc, Papakonstantinou, Georgios, Sundmacher, Kai, 2020. On the role of microkinetic network structure in the interplay between oxygen evolution reaction and catalyst dissolution. Sci. Rep. (ISSN: 2045-2322) 10 (1), 14140. http://dx.doi.org/10.1038/s41598-020-69723-3, URL http://www.nature.com/articles/s41598-020-69723-3.

Ding, Rui, Chen, Yawen, Rui, Zhiyan, Hua, Kang, Wu, Yongkang, Li, Xiaoke, Duan, Xiao, Wang, Xuebin, Li, Jia, Liu, Jianguo, 2022. Guiding the optimization of membrane electrode assembly in a proton exchange membrane water electrolyzer by machine learning modeling and black-box interpretation. ACS Sustain. Chem. Eng. 10 (14), 4561–4578. http://dx.doi.org/10.1021/acssuschemeng.1c08522, Publisher: American Chemical Society.

Dizon, Arthur, Fornaciari, Julie, Rochow, Maria, Weber, Adam Z., 2021. Sensitivity and effective parameterization of a multi-scale model of proton-exchange-membrane water electrolysis. ECS Trans. 104 (8), 417. http://dx.doi.org/10.1149/10408.0417ecst, ISSN 1938-5862. URL https://iopscience.iop.org/article/10.1149/10408.0417ecst/meta. Publisher: IOP Publishing.

Doan, Tuan Linh, Lee, Han Eol, Shah, Syed Shabbar Hassan, Kim, MinJoong, Kim, Chang-Hee, Cho, Hyun-Seok, Kim, Taekeun, 2021. A review of the porous transport layer in polymer electrolyte membrane water electrolysis. Int. J. Energy Res. (ISSN: 0363-907X, 1099-114X) 45 (10), 14207–14220. http://dx.doi.org/10.1002/er.6739, URL https://onlinelibrary.wiley.com/doi/10.1002/er.6739.

Espinosa-López, Manuel, Darras, Christophe, Poggi, Philippe, Glises, Raynal, Baucour, Philippe, Rakotondrainibe, André, Besse, Serge, Serre-Combe, Pierre, 2018. Modelling and experimental validation of a 46 kW PEM high pressure water electrolyzer. Renew. Energy (ISSN: 09601481) 119, 160–173. http://dx.doi.org/10.1016/j.renene.2017.11.081, URL https://linkinghub.elsevier.com/retrieve/pii/S0960148117311825.

Franco, Alejandro A., Gerard, Mathias, 2008. Multiscale model of carbon corrosion in a PEFC: Coupling with electrocatalysis and impact on performance degradation. J. Electrochem. Soc. (ISSN: 1945-7111) 155 (4), B367. http://dx.doi.org/10.1149/1.2838165, URL https://iopscience.iop.org/article/10.1149/1.2838165/meta. Publisher: IOP Publishing.

Franco, Alejandro A., Passot, Sylvain, Fugier, Pascal, Anglade, Christelle, Billy, Emmanuel, Guétaz, Laure, Guillet, Nicolas, Vito, Eric De, Mailley, Sophie, 2009. $Pt_x Co_y$ catalysts degradation in PEFC environments: Mechanistic insights: I. multiscale modeling. J. Electrochem. Soc. (ISSN: 1945-7111) 156 (3), B410B410. http://dx.doi.org/10.1149/1.3056048, URL https://iopscience.iop.org/article/10.1149/1.3056048/meta. Publisher: IOP Publishing.

Franco, A.A., Schott, P., Jallut, C., Maschke, B., 2007. A multi-scale dynamic mechanistic model for the transient analysis of PEFCs. Fuel Cells (ISSN: 1615-6854) 7 (2), 99–117. http://dx.doi.org/10.1002/fuce.200500204, URL https://onlinelibrary.wiley.com/doi/abs/10.1002/fuce.200500204. _eprint: https://onlinelibrary.wiley.com/doi/pdf/10.1002/fuce.200500204.

Franz, Tobias, Papakonstantinou, Georgios, Sundmacher, Kai, 2023. Transient hydrogen crossover in dynamically operated PEM water electrolysis cells - A model-based analysis. J. Power Sources (ISSN: 0378-7753) 559, 232582. http://dx.doi.org/10.1016/j.jpowsour.2022.232582, URL https://www.sciencedirect.com/science/article/pii/S0378775322015592.

Frei, S., Richter, T., 2020. Efficient approximation of flow problems with multiple scales in time. Multiscale Model. Simul. (ISSN: 1540-3459) 18 (2), 942–969. http://dx.doi.org/10.1137/19M1258396, ISSN: 1540-3467, URL https://epubs.siam.org/doi/10.1137/19M1258396.

Geiger, Simon, Kasian, Olga, Ledendecker, Marc, Pizzutilo, Enrico, Mingers, Andrea M., Fu, Wen Tian, Diaz-Morales, Oscar, Li, Zhizhong, Oellers, Tobias, Fruchter, Luc, Ludwig, Alfred, Mayrhofer, Karl J.J., Koper, Marc T.M., Cherevko, Serhiy, 2018. The stability number as a metric for electrocatalyst stability benchmarking. Nat. Catal. (ISSN: 2520-1158) 1 (7), 508–515. http://dx.doi.org/10.1038/s41929-018-0085-6, URL https://www.nature.com/articles/s41929-018-0085-6. Number: 7 Publisher: Nature Publishing Group.

Gorgun, H., 2006. Dynamic modelling of a Proton Exchange Membrane (PEM) electrolyzer. Int. J. Hydrog. Energy (ISSN: 03603199) 31 (1), 29–38. http://dx.doi.org/10.1016/j.ijhydene.2005.04.001, URL https://linkinghub.elsevier.com/retrieve/pii/S0360319905000868.

Gravemeier, V., Lenz, S., Wall, W.A., 2008. Towards a taxonomy for multiscale methods in computational mechanics: building blocks of existing methods. Comput. Mech. 41, 279–291.

Greening, Daniel R., 1990. Parallel simulated annealing techniques. Phys. D: Nonlinear Phenom. (ISSN: 0167-2789) 42 (1), 293–306. http://dx.doi.org/10.1016/0167-2789(90)90084-3, URL https://www.sciencedirect.com/science/article/pii/0167278990900843.

Grigor'ev, S.A., Khaliullin, M.M., Kuleshov, N.V., Fateev, V.N., 2001. Electrolysis of water in a system with a solid polymer electrolyte at elevated pressure. Russ. J. Electrochem. 37 (8), 819–822. http://dx.doi.org/10.1023/A:1016735003101.

Grigoriev, S.A., Kalinnikov, A.A., Millet, P., Porembsky, V.I., Fateev, V.N., 2010. Mathematical modeling of high-pressure PEM water electrolysis. J. Appl. Electrochem. (ISSN: 0021-891X) 40 (5), 921–932. http://dx.doi.org/10.1007/s10800-009-0031-z, ISSN: 1572-8838. URL http://link.springer.com/10.1007/s10800-009-0031-z.

Kasian, Olga, Grote, Jan-Philipp, Geiger, Simon, Cherevko, Serhiy, Mayrhofer, Karl J.J., 2018. The common intermediates of oxygen evolution and dissolution reactions during water electrolysis on iridium. Angew. Chem. Int. Ed. (ISSN: 1521-3773) 57 (9), 2488–2491. http://dx.doi.org/10.1002/anie.201709652, URL https://onlinelibrary.wiley.com/doi/abs/10.1002/anie.201709652. _eprint: https://onlinelibrary.wiley.com/doi/pdf/10.1002/anie.201709652.

Knöppel, Julius, Möckl, Maximilian, Escalera-López, Daniel, Stojanovski, Kevin, Bierling, Markus, Böhm, Thomas, Thiele, Simon, Rzepka, Matthias, Cherevko, Serhiy, 2021. On the limitations in assessing stability of oxygen evolution catalysts using aqueous model electrochemical cells. Nat. Commun. (ISSN: 2041-1723) 12 (1), 2231. http://dx.doi.org/10.1038/s41467-021-22296-9, URL http://www.nature.com/articles/s41467-021-22296-9.

Lautsch, Leopold, Richter, Thomas, 2021. Error estimation and adaptivity for differential equations with multiple scales in time. Comput. Methods Appl. Math. (ISSN: 1609-9389) 21 (4), 841–861. http://dx.doi.org/10.1515/cmam-2021-0030, URL https://www.degruyter.com/document/doi/10.1515/cmam-2021-0030/html. Publisher: De Gruyter.

Lebbal, M.E., Lecøeuche, S., 2009. Identification and monitoring of a PEM electrolyser based on dynamical modelling. Int. J. Hydrog. Energy (ISSN: 03603199) 34 (14), 5992–5999. http://dx.doi.org/10.1016/j.ijhydene.2009.02.003, URL https://linkinghub.elsevier.com/retrieve/pii/S0360319909002018.

Lin, Nan, Zausch, Jochen, 2023. 1D multiphysics modelling of PEM water electrolysis anodes with porous transport layers and the membrane. Chem. Eng. Sci. (ISSN: 0009-2509) 253, 117600. http://dx.doi.org/10.1016/j.ces.2022.117600, URL https://www.sciencedirect.com/science/article/pii/S0009250922001841.

Liu, QiXin, Jiang, PeiXue, Xiang, Heng, 2012. Experimental and molecular dynamics study of gas flow characteristics in nanopores. Chin. Sci. Bull. (ISSN: 1861-9541) 57 (13), 1488–1493. http://dx.doi.org/10.1007/s11434-012-5088-0.

Marangio, F., Santarelli, M., Calì, M., 2009. Theoretical model and experimental analysis of a high pressure PEM water electrolyser for hydrogen production. Int. J. Hydrog. Energy (ISSN: 0360-3199) 34 (3), 1143–1158. http://dx.doi.org/10.1016/j.ijhydene.2008.11.083, URL https://www.sciencedirect.com/science/article/pii/S0360319908016571.

Ni, Aleksey, Upadhyay, Mukesh, Shiva Kumar, S., Uwitonze, Hosanna, Lim, Hankwon, 2023. Anode analysis and modelling hydrodynamic behaviour of the multiphase flow field in circular PEM water electrolyzer. Int. J. Hydrog. Energy (ISSN: 0360-3199) 48 (43), 16176–16183. http://dx.doi.org/10.1016/j.ijhydene.2023.01.032, URL https://www.sciencedirect.com/science/article/pii/S0360319923000332.

Ogumerem, Gerald S., Pistikopoulos, Efstratios N., 2020. Parametric optimization and control for a smart Proton Exchange Membrane Water Electrolysis (PEMWE) system. J. Process Control (ISSN: 09591524) 91, 37–49. http://dx.doi.org/10.1016/j.jprocont.2020.05.002, URL https://linkinghub.elsevier.com/retrieve/pii/S0959152420302092.

Ojong, Emile Tabu, Kwan, Jason Tai Hong, Nouri-Khorasani, Amin, Bonakdarpour, Arman, Wilkinson, David P., Smolinka, Tom, 2017. Development of an experimentally validated semi-empirical fully-coupled performance model of a PEM electrolysis cell with a 3-D structured porous transport layer. Int. J. Hydrog. Energy (ISSN: 03603199) 42 (41), 25831–25847. http://dx.doi.org/10.1016/j.ijhydene.2017.08.183, URL https://linkinghub.elsevier.com/retrieve/pii/S0360319917334869.

Oliveira, Luiz Fernando L., Laref, Slimane, Mayousse, Eric, Jallut, Christian, Franco, Alejandro A., 2012. A multiscale physical model for the transient analysis of PEM water electrolyzer anodes. Phys. Chem. Chem. Phys. (ISSN: 1463-9084) 14 (29), 10215. http://dx.doi.org/10.1039/c2cp23300b, URL http://xlink.rsc.org/?DOI=c2cp23300b.

Olivier, Pierre, Bourasseau, Cyril, Bouamama, Pr. Belkacem, 2017. Low-temperature electrolysis system modelling: A review. Renew. Sustain. Energy Rev. (ISSN: 13640321) 78, 280–300. http://dx.doi.org/10.1016/j.rser.2017.03.099, URL https://linkinghub.elsevier.com/retrieve/pii/S136403211730432X.

Onda, Kazuo, Murakami, Toshio, Hikosaka, Takeshi, Kobayashi, Misaki, Notu, Ryouhei, Ito, Kohei, 2002. Performance analysis of polymer-electrolyte water electrolysis cell at a small-unit test cell and performance prediction of large stacked cell. J. Electrochem. Soc. (ISSN: 00134651) 149 (8), A1069. http://dx.doi.org/10.1149/1.1492287, URL https://iopscience.iop.org/article/10.1149/1.1492287.

Papakonstantinou, Georgios, Spanos, Ioannis, Dam, An Phuc, Schlögl, Robert, Sundmacher, Kai, 2022. Electrochemical evaluation of the de-/re-activation of oxygen evolving Ir oxide. Phys. Chem. Chem. Phys. 24 (23), 14579–14591. http://dx.doi.org/10.1039/D2CP00828A, URL https://pubs.rsc.org/en/content/articlelanding/2022/cp/d2cp00828a. Publisher: Royal Society of Chemistry.

Papakonstantinou, Georgios, Sundmacher, Kai, 2019. $H_2$ permeation through n117 and its consumption by IrOx in PEM water electrolyzers. Electrochem. Commun. (ISSN: 13882481) 108, 106578. http://dx.doi.org/10.1016/j.elecom.2019.106578, URL https://linkinghub.elsevier.com/retrieve/pii/S1388248119302413.

Prestat, Michel, 2023. Corrosion of structural components of proton exchange membrane water electrolyzer anodes: A review. J. Power Sources (ISSN: 0378-7753) 556, 232469. http://dx.doi.org/10.1016/j.jpowsour.2022.232469, URL https://www.sciencedirect.com/science/article/pii/S037877532201446X.

Qian, Xiao, Kim, Kangsan, Jung, Seunghun, 2022. Multiphase, multidimensional modeling of proton exchange membrane water electrolyzer. Energy Convers. Manage. (ISSN: 0196-8904) 268, 116070. http://dx.doi.org/10.1016/j.enconman.2022.116070, URL https://www.sciencedirect.com/science/article/pii/S0196890422008573.

Trinke, P., Bensmann, B., Hanke-Rauschenbach, R., 2017. Current density effect on hydrogen permeation in PEM water electrolyzers. Int. J. Hydrog. Energy (ISSN: 03603199) 42 (21), 14355–14366. http://dx.doi.org/10.1016/j.ijhydene.2017.03.231, URL https://linkinghub.elsevier.com/retrieve/pii/S0360319917312971.

Trinke, P., Bensmann, B., Reichstein, S., Hanke-Rauschenbach, R., Sundmacher, K., 2016. Hydrogen permeation in PEM electrolyzer cells operated at asymmetric pressure conditions. J. Electrochem. Soc. (ISSN: 0013-4651) 163 (11), F3164–F3170. http://dx.doi.org/10.1149/2.0221611jes, ISSN: 1945-7111. URL https://iopscience.iop.org/article/10.1149/2.0221611jes.

Virtanen, Pauli, Gommers, Ralf, Oliphant, Travis E., Haberland, Matt, Reddy, Tyler, Cournapeau, David, Burovski, Evgeni, Peterson, Pearu, Weckesser, Warren, Bright, Jonathan, van der Walt, Stéfan J., Brett, Matthew, Wilson, Joshua, Jarrod Millman, K., Mayorov, Nikolay, Nelson, Andrew R.J., Jones, Eric, Kern, Robert, Larson, Eric, Carey, C.J., Polat, Ilhan, Feng, Yu, Moore, Eric W., VanderPlas, Jake, Laxalde, Denis, Perktold, Josef, Cimrman, Robert, Henriksen, Ian, Quintero, E.A., Harris, Charles R., Archibald, Anne M., Ribeiro, Antônio H., Pedregosa, Fabian, van Mulbregt, Paul, SciPy 1.0 Contributors, 2020. SciPy 1.0: Fundamental algorithms for scientific computing in Python. Nature Methods 17, 261–272. http://dx.doi.org/10.1038/s41592-019-0686-2.

Voronova, Anastasiia, Kim, Hyoung-Juhn, Jang, Jong.Hyun, Park, Hee-Young, Seo, Bora, 2022. Effect of low voltage limit on degradation mechanism during high-frequency dynamic load in proton exchange membrane water electrolysis. Int. J. Energy Res. (ISSN: 1099-114X) 46 (9), 11867–11878. http://dx.doi.org/10.1002/er.7953, URL https://onlinelibrary.wiley.com/doi/abs/10.1002/er.7953. _eprint: https://onlinelibrary.wiley.com/doi/pdf/10.1002/er.7953.

Weinan, E., 2011. Principles of Multiscale Modeling. Cambridge University Press, ISBN: 978-1-107-09654-7.

Weinan, E., Engquist, Bjorn, 2003. The heterognous multiscale methods. Commun. Math. Sci. (ISSN: 1945-0796) 1 (1), 87–132. http://dx.doi.org/10.4310/CMS.2003.v1.n1.a8, URL https://www.intlpress.com/site/pub/pages/journals/items/cms/content/vols/0001/0001/a008/abstract.php. Publisher: International Press of Boston.

Weinan, E., Engquist, Bjorn, Li, Xiantao, Ren, Weiqing, Vanden-Eijnden, Eric, 2007. Heterogeneous multiscale methods: A review. Commun. Comput. Phys. (ISSN: 1815-2406) 2 (3), 367–450.

Weiß, A., Siebel, A., Bernt, M., Shen, T.-H., Tileli, V., Gasteiger, H.A., 2019. Impact of intermittent operation on lifetime and performance of a PEM water electrolyzer. J. Electrochem. Soc. (ISSN: 0013-4651) 166 (8), F487–F497. http://dx.doi.org/10.1149/2.0421908jes, ISSN: 1945-7111. URL https://iopscience.iop.org/article/10.1149/2.0421908jes.

Yang, Y., Jaeger, W., Neuss-Radu, M., Richter, T., 2016. Mathematical modeling and simulation of the evolution of plaques in blood vessels. J. Math. Biology 72, 973–996. http://dx.doi.org/10.1007/s00285-015-0934-8.

Yigit, Tevfik, Selamet, Omer Faruk, 2016. Mathematical modeling and dynamic Simulink simulation of high-pressure PEM electrolyzer system. Int. J. Hydrog. Energy (ISSN: 03603199) 41 (32), 13901–13914. http://dx.doi.org/10.1016/j.ijhydene.2016.06.022, URL https://linkinghub.elsevier.com/retrieve/pii/S0360319916318341.